

Capivara: A Spectral-based Segmentation Method for IFU Data Cubes

Rafael S. de Souza^{1,2*}, Luis G. Dahmer-Hahn^{3†}, Shiyin Shen³, Ana L. Chies-Santos⁴, Mi Chen³,
P. T. Rahna⁵, Renhao Ye³, Behzad Tahmasebzadeh⁶

¹ Centre for Astrophysics Research, University of Hertfordshire, College Lane, Hatfield, AL10 9AB, UK

² Instituto de Astronomia, Geofísica e Ciências Atmosféricas, USP, Rua do Matão 1226, 05508-090, São Paulo, Brazil

³ Shanghai Astronomical Observatory, Chinese Academy of Sciences, 80 Nandan Rd., Shanghai 200030, China

⁴ Instituto de Física Universidade Federal do Rio Grande do Sul Av. Bento Gonçalves 9500 Porto Alegre, R.S. 90040-060, Brazil

⁵ Centro de Estudios de Física del Cosmos de Aragón (CEFCA), Plaza San Juan 1, 44001 Teruel, Spain

⁶ Department of Astronomy, University of Michigan, 1085 S. University Ave., Ann Arbor, MI 48109, USA

Accepted XXX. Received YYY; in original form ZZZ

ABSTRACT

We present **CAPIVARA**, a fast and scalable multi-decomposition package designed to study astrophysical properties within distinct structural components of galaxies. Our spectro-decomposition code for analyzing integral field unit (IFU) data enables a more holistic approach, moving beyond conventional radial gradients and the bulge-plus-disk dichotomy. It facilitates comprehensive comparisons of integrated stellar ages and metallicities across various galactic structures. Our classification method naturally identifies outliers and organizes the different pixels based on their dominant spectral features. The algorithm leverages the scalability and GPU acceleration of Torch, outputting both a one-dimensional spectrum and a full data cube for each galaxy component, without relying on Voronoi binning. We demonstrate the capabilities of our approach using a sample of galaxies from the MaNGA survey, processing the resulting data cubes with the **STARLIGHT** spectral fitting code to derive both stellar population and ionized gas properties of the galaxy components. Our method effectively groups regions with similar spectral properties in both the continuum and emission lines. By aggregating the spectra of these regions, we enhance the signal-to-noise ratio of our analysis while significantly speeding up computations by reducing the number of spectra processed simultaneously. **CAPIVARA** is freely available on GitHub.

Key words: Data analysis-methods, galaxies: structure – galaxies: evolution

1 INTRODUCTION

Galaxies, the cosmic building blocks, comprise diverse stellar components such as bulges, disks, bars, spiral arms, and nuclear star clusters, each characterized by its age, metallicity, and kinematics (e.g., Hubble 1926; Tabor et al. 2017; Coccato et al. 2018; Johnston et al. 2022; Häußler et al. 2022; Nedkova et al. 2024; Jegatheesan et al. 2024; Lima-Dias et al. 2024; Zanatta et al. 2024).

The bulge of the Milky Way is notably ancient, exceeding 10 billion years in age, and is rich in metals. This contrasts with its disk, which exhibits metallicity closer to that of the Sun and a considerably younger average age (Hayden et al. 2015; Ness & Freeman 2016; Chiti et al. 2021). Upon detailed analysis, the Milky Way reveals thick and thin disks, a bar, spiral arms, a pseudo-bulge, and a halo (e.g., Anders et al. 2014; Helmi 2020; Queiroz et al. 2021; Ardern-Arentsen et al. 2024). Other models have been suggested to explain the formation of the Galactic disk, involving processes such as star formation, gas accretion, galaxy mergers, and stellar migration (Di Matteo 2016; Imig et al. 2023).

Unlike our Galaxy, such detailed scrutiny of structural components in galaxies beyond the Local Group is not possible, often leading to

crude divisions between disk and bulge components (Buitrago et al. 2008; Nedkova et al. 2024). Yet, the distinction between bulge and disk populations is pivotal for understanding the processes behind galaxy formation and evolution. It is generally accepted that massive galaxies form hierarchically in a simplified two-phase process: a rapid dissipative phase (which includes a starburst phase), followed by multiple mergers (Whitney et al. 2021). The James Webb Space Telescope is showing that massive galaxies are already in place at $z \sim 3$ (Carnall et al. 2023). Bulges are typically older and more metal-rich relative to disks (Lah et al. 2023). The influence of bulges and disks on galaxy evolution depends on factors like galaxy/halo mass, environment, and redshift (Conselice 2014; Cimatti et al. 2019). A galaxy’s environment (Peng et al. 2010b) also influences its properties (Lani et al. 2013; Lima-Dias et al. 2021), with central massive galaxies typically growing inside-out due to mechanisms like gas accretion and Active Galactic Nucleus (AGN) feedback, which predominantly impact central regions (e.g., Kim et al. 2011; Krumholz et al. 2018; Baker et al. 2023). Conversely, satellite galaxies often exhibit outside-in profiles due to external quenching forces that suppress star formation from the edges inward, a phenomenon understood by mechanisms such as major mergers (Lin et al. 2019; Cortese et al. 2021; Samuel et al. 2022). Recent findings of outside-in radial gradients in distant, low-mass satellites (Sandles et al. 2023)

* E-mail: r.da-silva-de-souza@herts.ac.uk

† E-mail: luisgdh@gmail.com

emphasize environmental quenching’s role from as early as $z = 2$. Alongside stellar histories, gas distribution and properties offer insights into quenching processes, with internal mechanisms leading to central outflows and environmental quenching leaving extended shocked gas distributions, identifiable by specific emission line ratios (Carniani et al. 2023).

Examining galaxies beyond the Local Group faces the challenge of not resolving individual stars, necessitating the use of models that approximate a galaxy’s light as stemming from a combination of single-age, single-metallicity populations (SSPs; see, e.g., Coelho et al. 2009; Coelho & Gadotti 2011; López-Corredoira et al. 2017; Pernet et al. 2024). Analyses of these properties often use photometric decomposition techniques on broad-band galaxy images. 2D photometric decomposition codes like GIM2D (Simard et al. 2002) and GALFIT (Peng et al. 2002, 2010a) are widely used and reveal the complex process of galaxy substructure formation and the distribution of different stellar populations.

The use of Integral Field Units (IFUs) has enabled more detailed studies of galaxy properties by providing simultaneous spectral and spatial information, allowing for the examination of chemical abundances and star formation histories in a spatially resolved manner. These observations have become an integral component of many low- and high-redshift surveys, including SAURON (Bacon et al. 2001), the Spectroscopic Imaging survey in the Near-infrared with SINFONI (SINS; Förster Schreiber et al. 2009), Mapping Nearby Galaxies at Apache Point Observatory (MaNGA; Bundy et al. 2015), Calar Alto Legacy Integral Field Area (CALIFA; Sánchez et al. 2012), and Middle Ages Galaxy Properties with Integral Field Spectroscopy (MAGPI; Foster et al. 2021).

IFU data have been used in bulge-disk decomposition to identify spaxels belonging to bulge- or disk-dominated regions, enabling the examination of the properties of the stellar populations in these regions. For example, Wisotzki et al. (2003) used 2D modeling techniques on IFU data to deblend the quadruple QSO and gravitational lens HE 0435-1223. A similar approach was used to separate the nuclear and host galaxy of the central region of 3C 120 (Sánchez et al. 2004) and to extract the deblended spectra of the galaxies in the core of Abell 2218 (Sánchez et al. 2007). A noteworthy package is the Bulge-Disk Decomposition of IFU data (BUDDI; Johnston et al. 2017), which utilizes GALFITM (Häußler et al. 2013), a modified version of GALFIT (Peng et al. 2002, 2010a), to model the light profile of multi-wavelength images of a galaxy. Méndez-Abreu et al. (2019) employed C2D, a multi-component decomposition, which consists of fitting a galaxy’s surface-brightness distribution at each wavelength (quasi-monochromatic image) via a 2D photometric decomposition code.

One limitation of current image decomposition methods is their reliance on preset categories like halos, bulges, disks, bars, and rings, leaving out structures that don’t fit these categories, such as asymmetric features. Additionally, when working with IFUs, these methods typically treat each wavelength independently rather than as part of a high-dimensional tensor, potentially overlooking important correlations—such as those between bluer wavelengths and H I emission. This results in the loss of useful information that could provide insights into the physical mechanisms behind these features.

This work explores an alternative approach for spectral categorization of different physical regions in galaxies. Instead of using pre-conceived 2D profile models, our method employs a non-parametric, multi-component decomposition based solely on *spectral similarity*. This allows for greater flexibility in decomposing complex structures, such as those found in mergers and irregular galaxies. By utilizing *unsupervised hierarchical clustering*, our approach directly targets

the wavelength space instead of treating the data cube as a stack of images at each wavelength. This methodology leverages torch (Paszke et al. 2019), a deep learning library designed for tensor computations and GPU acceleration, enabling fast and efficient matrix calculations. Its capabilities make it particularly suitable for the decomposition of large datasets, offering a powerful tool for the analysis of IFU data cubes.

This paper is organized as follows: In Section 2, we provide a detailed description of our method. Section 3 briefly describes the data used in our study. In Section 4, we demonstrate the practical application of our code on five MaNGA galaxies. We compare our approach with existing methods from the literature and present our conclusions in Section 5.

2 METHOD: SPECTRO-DECOMPOSITION

Our model classifies each IFU pixel $\phi = \{\phi_i \in \mathbb{R}^{x \times y \times w}\}_{i=1}^N$ into C clusters, ensuring that spectra within a cluster are similar, while those in different clusters are dissimilar. Here, N denotes the total number of pixels ($x \times y$), and w is the number of spectral channels. We measure similarity using the ℓ_2 distance metric, given by:

$$\ell_p(x, y) = \left(\sum_{i=1}^d |x_i - y_i|^p \right)^{\frac{1}{p}}, \quad (1)$$

where $p = 2$ represents the Euclidean distance. Here, x and y represent two independent vectors of features, i is the index of the feature, and d is the number of features. In our case, the features are the flux values at each wavelength bin of the IFU. While other possible choices exist, such as the Kullback–Leibler divergence (Kullback & Leibler 1951), mutual information (Li 1990), and so forth, we opt for the ℓ_2 norm due to its simplicity and its relation to χ^2 statistics, a standard method for spectral fitting and template matching. This approach preserves the common underlying assumption that spectra can be compared via their respective Euclidean distances. The properties of the spectra include their overall shape, the strength of particular spectral lines, and other distinguishing characteristics that can influence the similarity measure.

Once the similarity measure, in the form of a distance matrix, is established, the algorithm begins by assigning each spectrum from a given spaxel to its own group. This initial step ensures that each spectrum is considered a unique entity, facilitating a more granular analysis. The algorithm then proceeds iteratively, merging the two most similar clusters in each iteration until a predetermined number of groups is achieved. This process of successive merging can be visualized as the construction of a hierarchical tree, where groups formed by merging similar spectra are placed lower on the tree, and those that are less similar are positioned higher.

One of the significant advantages of hierarchical clustering is its ability to detect associations at various levels of granularity (e.g. Murtagh & Legendre 2014; de Souza et al. 2023). For example, to identify broad categories of galaxy spectra like star-forming and passive galaxies, the algorithm can cut the tree at a higher level in the hierarchy, leading to fewer, broader groups. Conversely, for more specific distinctions within a category of galaxy spectra, we can cut the tree at a lower level, resulting in finer-grained groups. This approach allows for a hierarchical tree with broad categories at the higher levels and more specific subcategories at the lower levels. We note that during the writing of our work, independent groups have also pursued the idea of an unsupervised approach to cluster regions of similar spectra, but using a different methodology

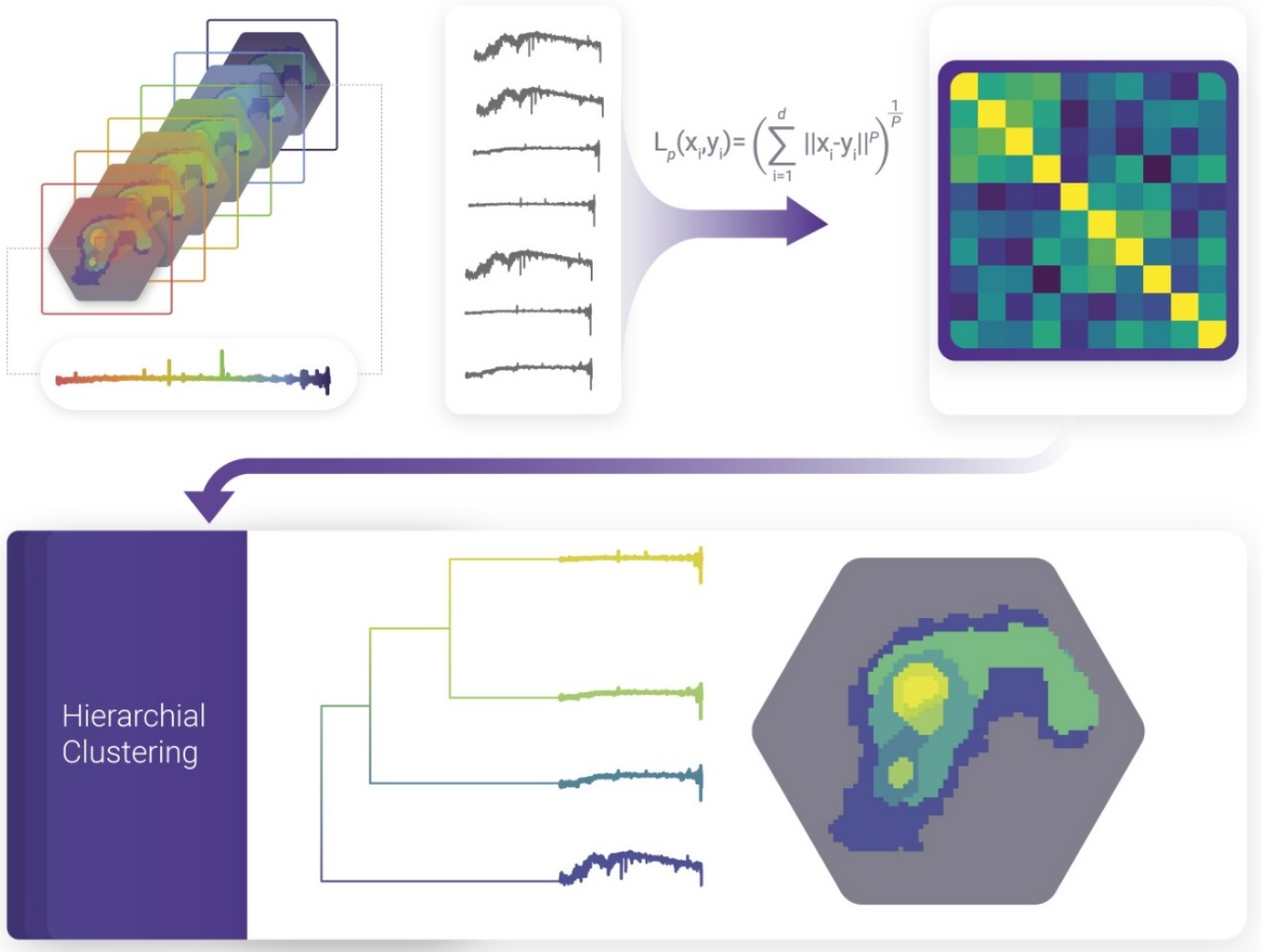


Figure 1. Workflow illustration of our spectro-based segmentation method. The model reads an IFU data cube composed of multiple wavelength channels, each represented by a slice in the left image. Hierarchical clustering is then performed on the dissimilarity matrix computed from pairwise distances between all spectra within the cube. Once the groups are assigned, the data is back-transformed into a 2D matrix where each group represents spectra with similar features. This process identifies galactic structures through spectral characteristics, enabling a refined structural decomposition.

based on the Fisher Expectation-Maximization algorithm (Chambon & Fraix-Burnet 2024).

The general workflow of our approach is depicted in Fig. 1. Consider a hypothetical data cube with dimensions $64 \times 64 \times 1,000$, where the first two dimensions represent the spatial resolution in pixels, and the last dimension represents the number of sampled wavelengths in the spectra. The 64×64 spectra are transformed into a matrix with 1,000 columns and 64×64 rows, where each row represents a particular spaxel and each column represents a wavelength. On this matrix, we perform a pairwise distance estimate, which yields a dissimilarity matrix of size $4,096 \times 4,096$, where each cell represents the dissimilarity between pairs of spaxels. We then apply the hierarchical clustering model on the dissimilarity matrix, assigning each set of spectra to a particular group. Once this procedure is completed, we back-transform the list of spectral-based groups into their respective original spatial positions. The output will then be a 64×64 FITS file with an assigned group for each matrix element, which is depicted by the rightmost panel of Fig. 1.

To decide the number of groups, we suggest a heuristic approach. If the goal is to separate the galaxy into bulge and disk components,

two groups are often sufficient, assuming we disregard the group corresponding to the sky background. However, if the aim is to detect regions with different star-formation histories or ionization mechanisms, an increasing number of components should be used. If the objective is to increase the signal-to-noise ratio without losing information, the number of components must account for the spatial resolution, bin size, and field of view of the data. Therefore, we recommend using a sufficiently large number of groups that remain manageable for running a spectral fitting code of choice.

3 MANGA IFU DATA

To showcase our approach, we use data from the MaNGA IFU survey—a major observational campaign of the Sloan Digital Sky Survey IV (SDSS-IV; Blanton et al. 2017) that aimed to study the internal kinematics and chemical properties of a large sample of nearby galaxies. It is the largest IFU survey of nearby galaxies to date, using the BOSS spectrograph to obtain spatially resolved spectroscopic data for approximately 10,000 galaxies in the redshift range

$0.01 < z < 0.15$ (typical $z \sim 0.03$). The survey uses custom fiber bundles with a core diameter of $2''.0$ and IFUs ranging from 19 to 127 fibers, providing a field of view from $12''.0$ to $32''.0$. The spectra have a wavelength coverage of $3,622\text{--}10,354 \text{ \AA}$ and a spectral resolution of $R \sim 2,000$. MaNGA obtains three dithered exposures for each target galaxy. The data cube has a spatial scale of 0.5 arcseconds per pixel and varies in the number of wavelength channels based on the sampling method used. The MaNGA data cube contains 4,573 channels for logarithmic sampling and 6,732 channels for linear sampling (Law et al. 2016).

4 ANALYSIS OF FIVE MANGA GALAXIES

We demonstrate the feasibility of our method for identifying regions with different spectral properties within an extended object by selecting a sample of five morphologically diverse galaxies from MaNGA. The main properties of each galaxy, as listed in Table 1, were obtained from NED¹ and Marvin². Our sample includes spiral, elliptical, and merger galaxies, as well as various features such as bars, rings, and individual stars in the field.

After running CAPIVARA on the MaNGA data cubes, we obtained a matrix for each galaxy, assigning each pixel to its respective group. Fig 2 shows, in the top row, a *gri* composite image of the five chosen galaxies in our sample. In the bottom row, we show the spatial distribution of the 20 components detected by CAPIVARA. The color scheme is qualitative since the components are not ordered in any continuous scale³

A visual inspection of these figures reveals several interesting features. For example, our method effectively identifies the merger structure directly from the data cubes for the galaxy 7443-12703 (VV 705), a binary merger system in the constellation of Bo tes (Rupke & Veilleux 2013; Larson et al. 2016), with a nuclear separation of approximately 6–7 kpc and featuring long tidal tails ($\sim 40''$).

In the case of the spiral galaxies UGC 3907 (8135-12701) and MCG+05-22-014 (11749-12701), located in the constellations of Lynx and Cancer, respectively, our approach isolates what is most likely a foreground star, eliminating the need to mask the cube before further analysis, as is standard procedure in the Data Analysis Pipeline for MaNGA (Westfall et al. 2019). For the spiral galaxy MCG+00-07-007 (10224-6104), located in the constellation Cetus, the model detects at least three distinct spots, which we will further discuss as representing different stellar populations. These results illustrate the method’s efficiency in isolating foreground elements and detecting key structural components of the galaxy with minimal pre-processing.

We note that this initial analysis should be taken as a proof of concept since we are using the entire wavelength range of the spectra for clustering. For case-specific applications, we advise selecting specific ranges of the spectra to achieve a more domain-specific segmentation. Below, we show a continuum and emission line analyses to compare the results before and after decomposition.

4.1 Continuum classification

Stellar population synthesis involves several steps: first, the observed galaxy spectrum is cleaned and calibrated to remove noise and er-

rors. The spectrum is then divided into wavelength bins, and flux is measured in each bin. Finally, the observed spectrum is fitted with theoretical templates derived from galaxy evolution models, stellar libraries, and initial mass functions to analyze the continuum.

The fitting process minimizes the χ^2 between observed and modeled spectra, considering factors like dust reddening and kinematics. Once the best-fit template is identified, the galaxy’s physical properties can be inferred. For instance, redshift is determined from the shift in spectral features, while luminosity is derived from the overall flux. The star formation history is deduced from the strengths of various absorption and emission lines. By evaluating the contributions of different templates, we can also infer properties such as age, and metallicity. Prior to the fitting, spurious features and emission lines are masked to ensure a more accurate study on the stellar continuum.

We employed the STARLIGHT code (Cid Fernandes et al. 2004, 2005), which fits observed spectra using a model library that accounts for kinematics and dust reddening. We utilized the E-MILES library of SSP models (Vazdekis et al. 2016), based on a revised Kroupa (2001) initial mass function and BaSTI isochrones (Pietrinferni et al. 2004, 2006). This library spans from 1680 to 50,000 \AA , with an optical resolution of 2.5 \AA . STARLIGHT has been rigorously tested across multiple IFS galaxy surveys; for an application to MaNGA data, see Mallmann et al. (2018). Since CAPIVARA outputs are in FITS format, any spectral fitting method can easily be applied to extract stellar and ionized-gas properties from our galaxy structures.

To expedite our analysis, we restricted our library to 10 representative ages⁴ and 3 representative metallicities⁵. We also included a featureless continuum (FC) with $F_\nu \propto \nu^{-1.5}$ to account for potential AGN emission, as well as very young (< 5 Myr) SPs, which are indistinguishable from AGN-type continua (Storchi-Bergmann et al. 2000; Riffel et al. 2009). Caution is therefore advised when interpreting this component. Figure 3 shows the integrated observed spectra of each galaxy in black, with the corresponding STARLIGHT model spectra in red.

Since small differences in stellar population composition are often obscured by noise present in real data (Cid Fernandes et al. 2004, 2005; Riffel et al. 2009), we grouped the SSP models into four age bins: young (*xy*: ≤ 100 Myr), young-intermediate (*xyi*: 0.1–0.7 Gyr), intermediate-old (*xio*: 0.7–2 Gyr), and old (*xo*: 2–13 Gyr). This categorization helps capture major evolutionary phases while accounting for the noise limitations in the data.

In Figs. 4 to 5, we present the light fraction of the FC for each age bin. The top row shows the results before decomposition, while the bottom row displays the results after decomposition. Our method effectively identifies the main regions in each galaxy, preserving their distinct features. For the galaxy 7443-12703, our code successfully identified two regions with younger stellar populations and stronger FC contributions: one concentrated in the nucleus and another located $4''.0$ East and $8''.0$ North of the nucleus. Additionally, it accurately grouped the semi-ring structure observed in the *xy* age bin panel. In the galaxy 8135-12701, our method identified the bulge and disk regions, with the bulge dominated by an old stellar population (SP) and the disk primarily by intermediate-age SPs. Additionally, it detected a spiral arm with higher FC contributions compared to the rest of the galaxy, visible in the upper left region of 8135-12701 FC panel. This FC component likely originates from very young SPs in the spiral arms, as there is no evidence of AGN activity in this galaxy.

Galaxy 8443-6102, the only early-type galaxy in our sample, ex-

¹ <http://ned.ipac.caltech.edu/>

² <https://dr17.sdss.org/marvin/>

³ The color palette for this figure was created using Vincent van Gogh’s *The Starry Night* painting as inspiration.

⁴ 0.03, 0.06, 0.1, 0.3, 0.6, 1.0, 3.0, 6.0, 10.0, and 13.0 Gyrs

⁵ $Z = 0.0040, 0.0198, \text{ and } 0.0400 Z_\odot$

MaNGA ID	Name	RA	Dec	z	Type	Diameter [kpc]
7443-12703	VV 705 (IRAS F15163+4255)	229.525	42.745	0.0403	Merger	47.91
8135-12701	UGC 3907	113.472	37.025	0.0618	SABc	111.32
8443-6102	UGC 8730	207.061	24.777	0.0274	(R)SB0	45.49
10224-6104	MCG +00-07-007	35.624	0.383	0.0248	Spiral	17.85
11749-12701	MCG+05-22-014	138.318	31.358	0.0417	Sc	59.80

Table 1. Basic properties of our galaxy sample.

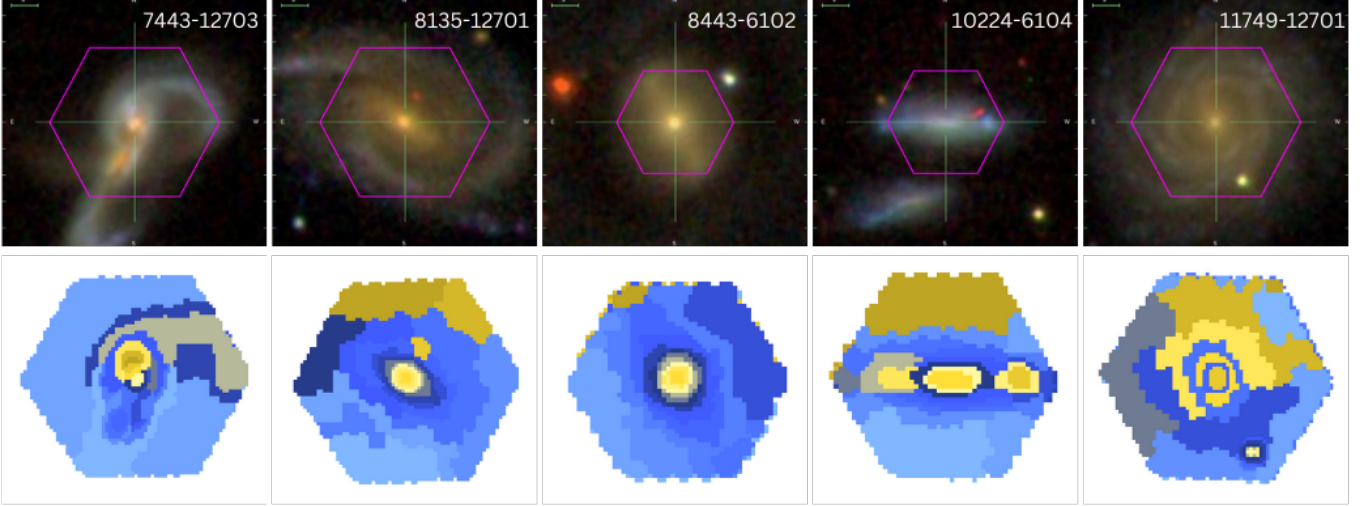


Figure 2. **Top row:** SDSS images of five galaxies in our sample, with the MaNGA plate numbers indicated in the upper right corner of each image. The field of view of the IFU (Integral Field Unit) is overlaid in purple. **Bottom row:** Spatial distribution maps of components detected by CAPIVARA in the same galaxies. The color gradients represent the varying intensities of each detected component, as derived from spectral analysis. Each map provides insights into the morphological and structural properties captured by the segmentation algorithm.

hibits the simplest stellar population structure. It consists of an older central region and outer areas within our Field of View (FoV), where a small FC contribution ($\sim 10\%$) was detected. Additionally, a subtle ring-like structure with a slightly younger stellar population is present. Our method accurately identified all these regions, particularly the faint ring-like structure, which is barely visible in the old age bin panel. Unlike 8443-6102, 10224-6104 displays a complex structure with three distinct light centers and an uneven stellar population. The rightmost light source is dominated by an FC-type continuum, the leftmost by a young stellar population, and the central, brightest source by a young-intermediate stellar population. CAPIVARA was able to detect each light source and group their influence regions together, highlighting these differences. Additionally, a fourth region with a different continuum composition was detected in the left edge of our FoV, showing a slightly higher FC contribution if compared to its surroundings.

Our final object, 11749-12701, is especially notable because, despite its simple stellar population—featuring an old bulge and younger outskirts—a field star is also present. Using our approach, we automatically identified the galaxy’s structures and separated the field star from the rest of the FoV.

4.2 Emission lines classification

After subtracting the stellar spectra derived in section 4.1, we measured the flux of the four main emission lines ($H\alpha$, $H\beta$, $[\text{N II}]\lambda 6583\text{\AA}$ and $[\text{O III}]\lambda 5007\text{\AA}$) required to build the Baldwin-Phillips-Terlevich diagram (BPT; Baldwin et al. 1981; Veilleux & Osterbrock 1987;

Rola et al. 1997; Kewley et al. 2001; Kauffmann et al. 2003; Stasińska 2007; Schawinski et al. 2010). This analysis was conducted by fitting a Gaussian function to each emission line using the IFSCUBE code (Ruschel-Dutra et al. 2021). IFSCUBE fits multiple Gaussian or Gauss-Hermite profiles, with or without constraints, and supports pixel-by-pixel uncertainties, weights, flags, and pseudo-continuum fitting. The best fit is determined by minimizing the χ^2 , with free parameters being the amplitude, radial velocity, and velocity dispersion of each component. Our sample galaxies exhibited no signs of multiple components per emission line, and a single narrow Gaussian was sufficient. Given the similar ionization potentials of $H\alpha$, $H\beta$ and $[\text{N II}]$ have similar ionization potentials, their kinematic properties were fixed, while $[\text{O III}]$ was allowed independent radial velocity and velocity dispersion. Fig 6, provides an example fit for galaxy 10224-6104 at $(10'0, 0'0)$.

The $H\alpha$, $H\beta$, $[\text{N II}]$, and $[\text{O III}]$ maps are displayed in Figures 7 and 8. From left to right, the panels depict the fluxes for $[\text{O III}]$, $H\beta$, $[\text{N II}]$, and $H\alpha$. The top row presents the fluxes measured from the original data cube, while the bottom row shows the measurements after running CAPIVARA. Similar to the stellar continuum, our method effectively identifies the main emission-line regions in each object. However, the improvement in S/N is much more pronounced in the emission lines. In many regions of the original datacube, these features are not properly measured due to not meeting the S/N threshold. This issue is resolved in the decomposed datacube, where our model not only enhances the S/N and correctly groups the regions but also ensures more consistent and accurate measurements of these features,

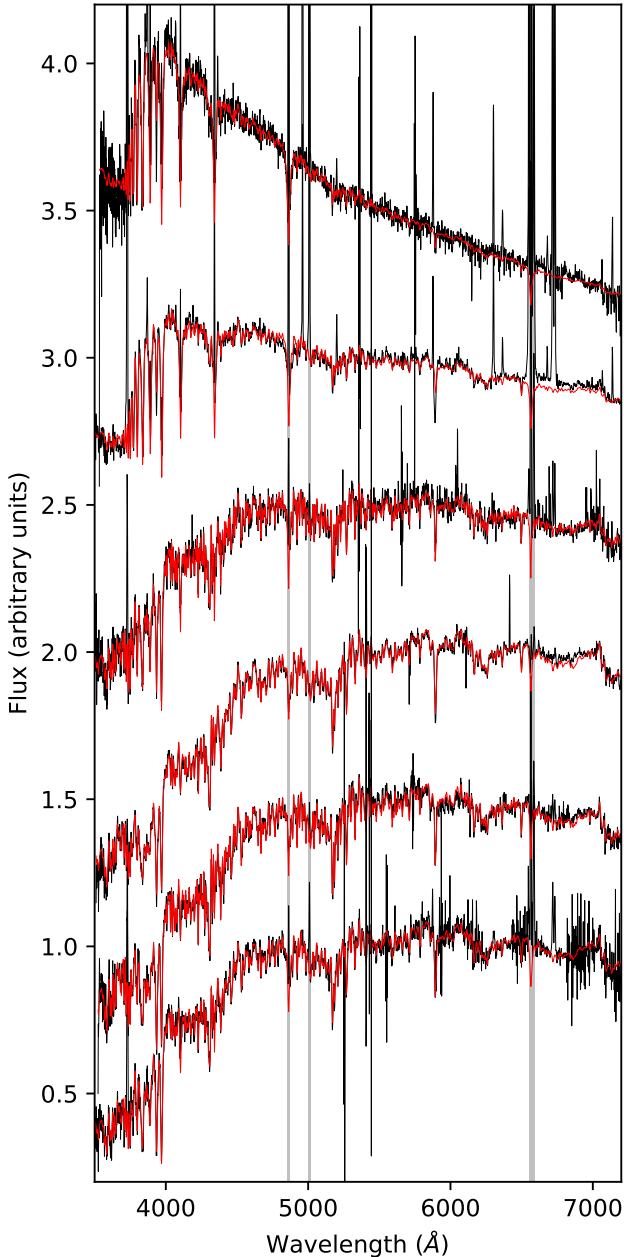


Figure 3. Observed (black) and modeled (red) integrated spectra of our sample galaxies are shown. Grey-shaded regions correspond to the areas integrated to construct the BPT diagram. For better visualization, we present these spectra in order of inclination. From top to bottom: 10224-6104, 7443-12703, 11749-12701, 9039-9102, 8443-6102, and 8135-12701.

without merging regions that are not physically meaningful from a spectral perspective.

In our sample, regions identified by their distinct continuum properties also exhibit differences in emission line properties, so the figures typically highlight the same regions discussed in Section 4.1. However, even when two regions share similar continuum properties but differ in their emission lines, or vice versa, our approach should be able to separate them effectively. Moreover, depending on the spectral features being studied, different techniques can be applied. For instance, when focusing on the stellar continuum, our method can

be performed on the original datacube since there are significantly more continuum points than emission line points. Alternatively, if the study targets emission lines, one can analyze the derivative of the original datacube. In regions where the continuum dominates, the derivative will be close to zero, whereas in areas dominated by complex emission lines, it will deviate significantly from zero.

In this way, *CAPIVARA* can be tailored to focus on specific features of interest, classifying different regions of the galaxy based on those chosen features. Since this paper focuses on the methodology rather than specific astrophysical cases, which will be addressed in follow-up papers, we performed both continuum and emission line analyses based on the initial decomposition into 20 distinct regions. Even with this straightforward approach, the characteristics of the original object were successfully recovered, showcasing the simplicity and efficacy of our method.

4.3 Continuum and emission line spectral classification

Although the same galaxy can be classified into different categories based on ad hoc criteria or specific predetermined wavelength windows, a general sanity check for *CAPIVARA* is to ensure that its spectral segmentation is qualitatively consistent with traditional continuum and emission line-based classifications. To achieve this, we classified each representative spectrum based on both continuum features and emission line characteristics.

Based on the dominant stellar populations in each object, we divided our sample into six classes: AGN, star-forming (SF), post-starburst (PS), intermediate-age (IA), mixed (MIX), and quenched (QUENCH). The AGN class includes objects dominated by a power-law-like spectrum, while the star-forming class includes objects dominated by simple stellar populations (SSPs) younger than 100 Myr. The post-starburst class consists of objects dominated by SSPs between 100 and 700 Myr, while the intermediate-age class consists of SSPs between 700 Myr and 2 Gyr. The mixed class includes objects where SSPs older than 2 Gyr contribute less than 40% of the luminosity, and the quenched class includes objects where SSPs older than 2 Gyr contribute more than 40% of the luminosity.

The BPT diagram classifies galaxies into five distinct categories based on their emission line fluxes: inactive (INACT), star-forming (SF), composite or transition (TRANSIT), low-ionization nuclear emission-line region (LINER), and Seyfert galaxies. It utilizes the flux ratios of $H\beta$, $[OIII] \lambda 5007$, $H\alpha$, and $[NII] \lambda 6583$, plotting galaxies in a parameter space defined by $\log([NII]/H\alpha)$ on the x-axis and $\log([OIII]/H\beta)$ on the y-axis. The thresholds between these line ratios, as defined by Kewley et al. (2001) and Kauffmann et al. (2003), are used to differentiate between these classes. Inactive galaxies are identified by $[OIII]$ emission below 3σ of the continuum signal-to-noise ratio (S/N). Star-forming galaxies, primarily influenced by photoionization from young, hot stars, exhibit low values of both $[NII]/H\alpha$ and $[OIII]/H\beta$, occupying the left wing locus of the BPT diagram. In contrast, AGN-dominated galaxies, including LINERs and Seyferts, lie on the opposite side. LINERs display high $[NII]/H\alpha$ but low $[OIII]/H\beta$ ratios, with their ionization source being uncertain, possibly due to nuclear activity or evolved stellar populations. Seyferts show high values in both $[NII]/H\alpha$ and $[OIII]/H\beta$ ratios. Finally, the transition class falls in the zone between star-forming and AGN objects, demarcated by the theoretical extreme starburst line proposed by Kewley et al. (2001) and the empirical starburst line by Kauffmann et al. (2003).

Figure 9 shows the classification maps for our five galaxies. The first two panels on the left in each row display the maps for the continuum classes, while the two panels on the right present the classification

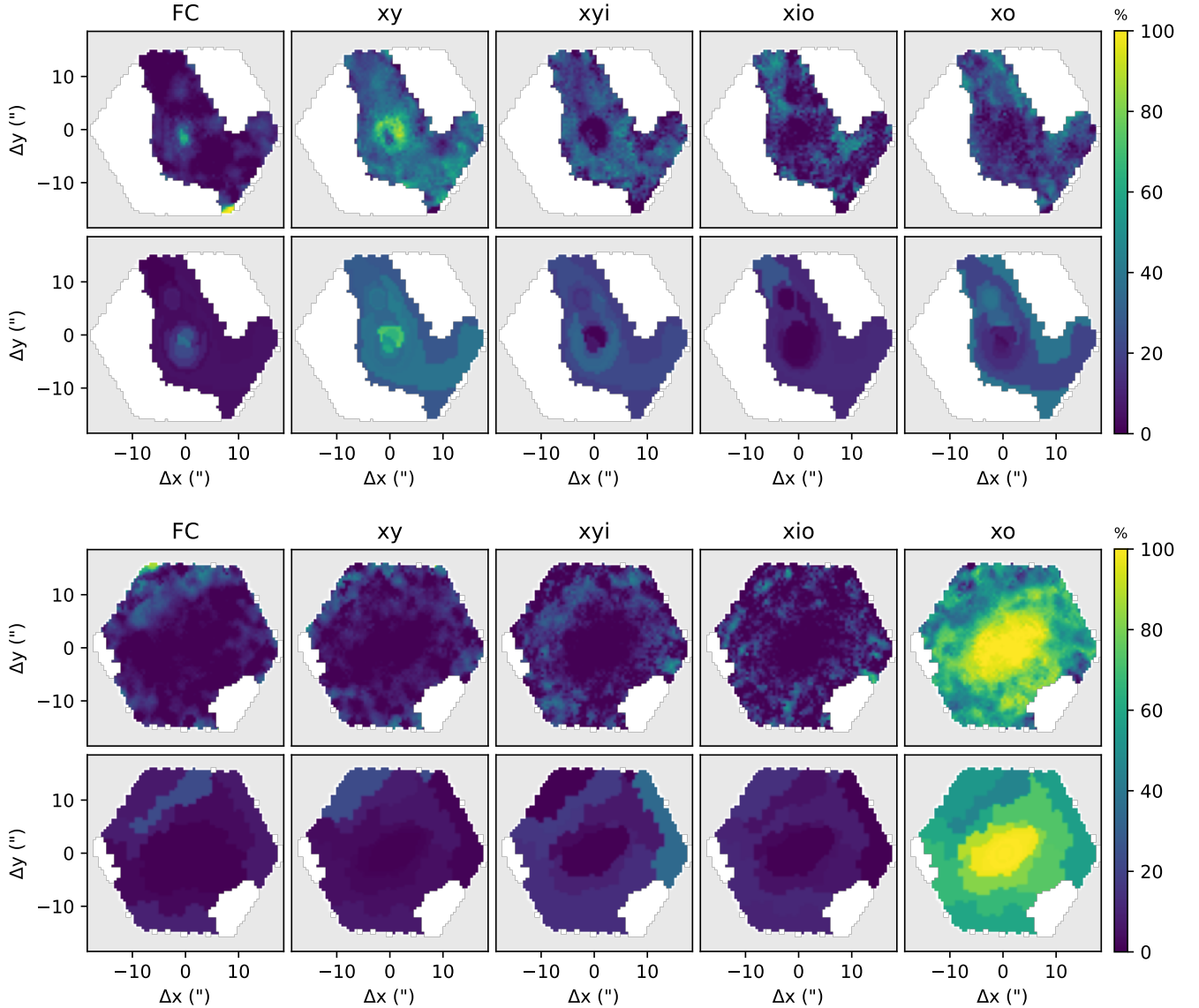


Figure 4. Stellar population demographics for 7443-12703 (top) and 8135-12701 (bottom). **Top row** in each set: Regions derived from the original data cube. **Bottom row** in each set: Results from the decomposed data cube using `CAPIVARA`. The categories, from left to right, are featureless continuum (FC), young (xy: ≤ 100 Myr), young-intermediate (xyi: 0.1-0.7 Gyr), intermediate-old (xio: 0.7-2 Gyr), and old (xo: 2-13 Gyr) stellar populations. The color bar indicates the fractional contribution of each age bin to the total light, with brighter colors representing higher contributions.

based on emission lines. In both cases, the original datacube is shown first, followed by the decomposed datacube. Although a more detailed analysis of subtle differences is beyond the scope of this initial paper, we note an overall agreement between the segmented regions detected by `CAPIVARA` and the predefined classes. Future studies will aim to refine this approach, tailoring it to more domain-specific cases.

5 CONCLUSIONS

Traditional methods for analyzing astronomical data cubes often struggle to extract full signals from noisy backgrounds, particularly when astrophysical or instrumental correlations between nearby measurements are underestimated. To address these challenges, efforts have been made to incorporate spatial information, such as global parametric models for physical distributions in kinematic studies

(e.g., [Krajnović et al. 2006](#); [Watkins et al. 2013](#)) and automated spatial segmentation ([Casado et al. 2017](#)). One common approach to improve signal-to-noise ratio (S/N) is through adaptive binning techniques like Voronoi tessellation ([Cappellari & Copin 2003](#)), which groups spaxels into contiguous regions for averaged measurements ([Sanders & Fabian 2001](#); [Diehl & Statler 2006](#); [Sánchez et al. 2016](#)). While these techniques enhance statistical confidence, they often do so at the expense of spatial resolution.

Our method, however, takes a different approach. Primarily designed to decompose data into regions with distinct physical properties, it naturally enhances the S/N as a secondary benefit. In contrast to Voronoi binning, which focuses on data quality by merging regions that may have different physical properties, our approach ensures that only regions with similar characteristics are grouped. In our current

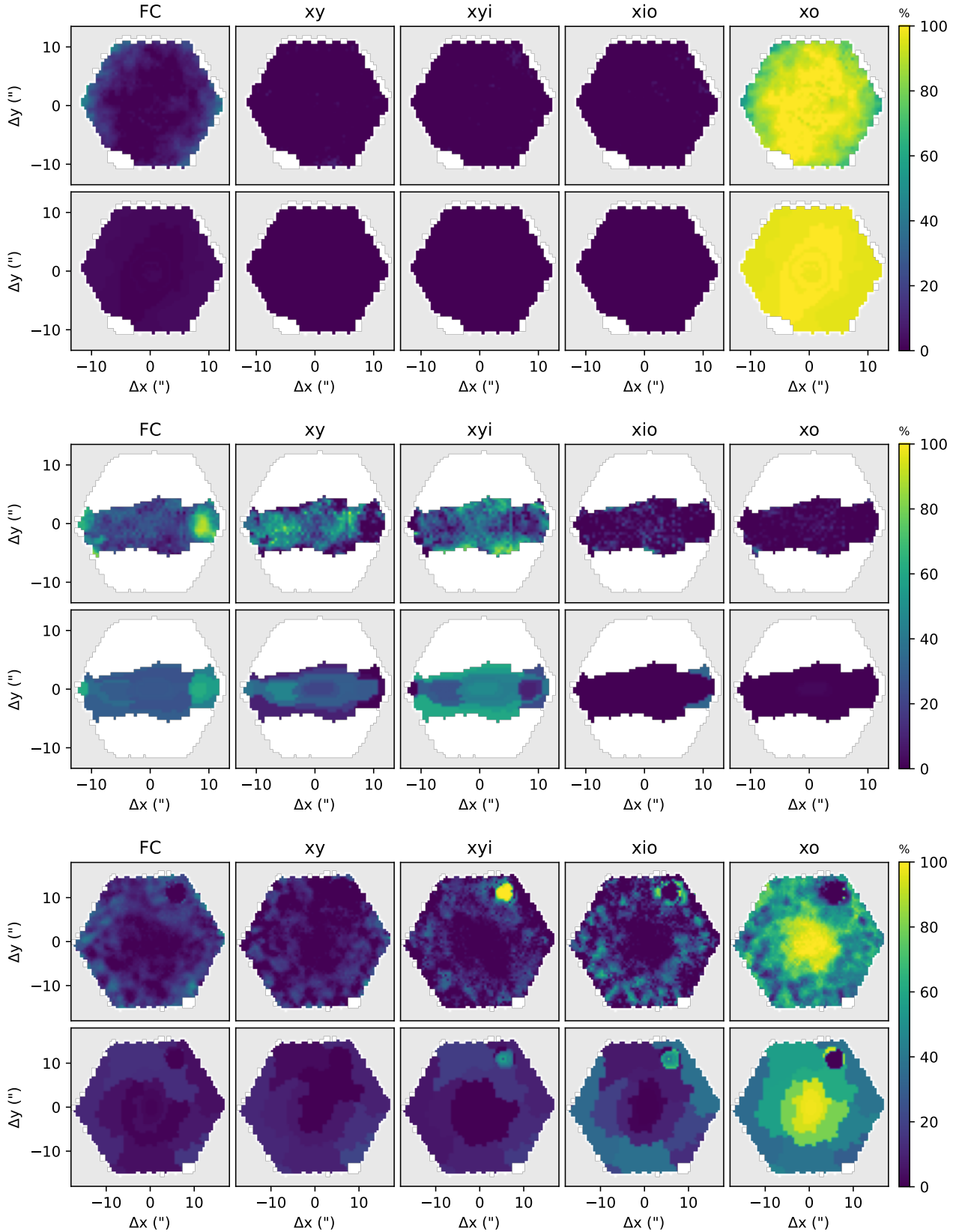


Figure 5. Stellar population demographics for 8443-6102 (top), 10224-6104 (middle), and 11749-12701 (bottom). **Top row** in each set: Regions derived from the original data cube. **Bottom row** in each set: Results from the decomposed data cube using `CAPIVARA`. The categories, from left to right, are featureless continuum (FC), young (xy : ≤ 100 Myr), young-intermediate (xyi : 0.1-0.7 Gyr), intermediate-old (xio : 0.7-2 Gyr), and old (xo : 2-13 Gyr) stellar populations. The color bar indicates the fractional contribution of each age bin to the total light, with brighter colors representing higher contributions.

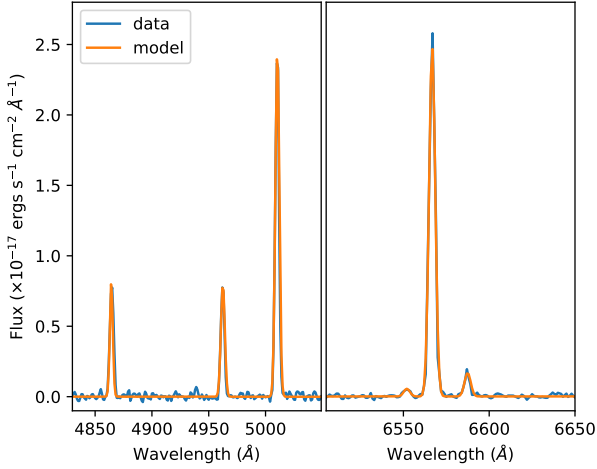


Figure 6. Fitting example for the $(10'0, 0'0)$ spaxel of 10224-6104. Each emission line was fitted with a single Gaussian profile.

analysis, decomposing the data cube into 20 distinct regions results in a five-fold improvement in S/N compared to individual spectra.⁶

Building on this, we introduce *CAPIVARA*, a novel spectral-based segmentation method for IFU data cubes. Designed specifically to enhance the study of structural properties in galaxies, *CAPIVARA* employs hierarchical clustering in the spectral domain, grouping similar spectra to improve S/N without compromising astrophysical similarity among regions.

In a demonstration using five selected MaNGA galaxies, *CAPIVARA* identified and grouped regions with similar physical properties. These groupings were validated against standard methods for stellar continuum and gas property analysis. By providing both decomposed data cubes and integrated one-dimensional spectra for each region, *CAPIVARA* facilitates a more detailed investigation of stellar and ionized gas properties.

ACKNOWLEDGEMENTS

LGDH acknowledges support by National Key R&D Program of China No.2022YFF0503402, and National Natural Science Foundation of China (NSFC) project number E345251001.

DATA AVAILABILITY

This work uses data from the MaNGA DR17 data release, available at <https://www.sdss4.org/dr17/manga/>.

⁶ This estimate was derived from the continuum between 5500 and 5600 Å, chosen for its minimal stellar absorption and emission lines.

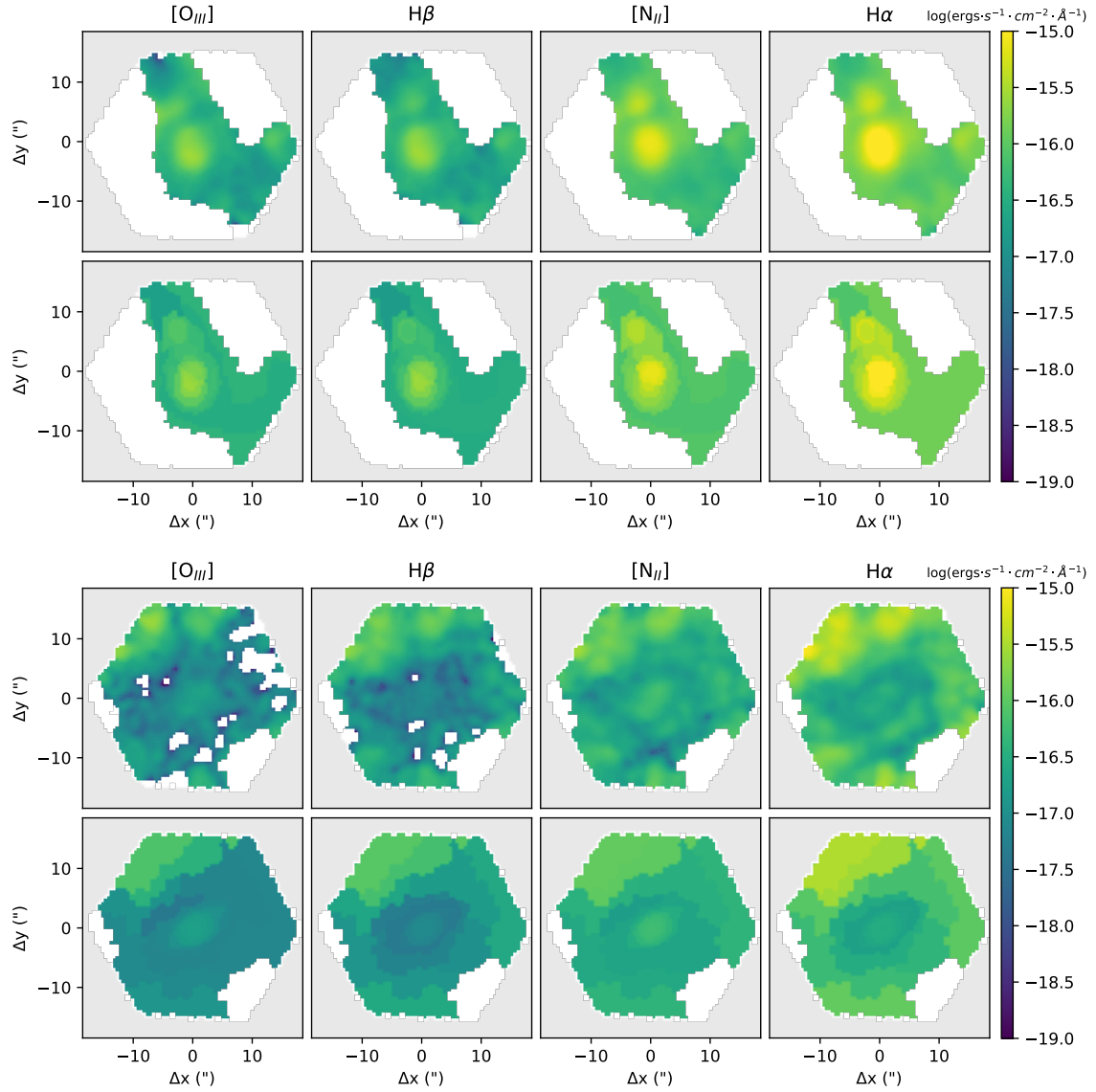


Figure 7. Logarithmic fluxes of the four main emission lines for 7443-12703 (top) and 8135-12701 (bottom), in $\text{ergs}\cdot\text{s}^{-1}\cdot\text{cm}^{-2}\cdot\text{\AA}^{-1}$. **Top row** in each set: Fluxes measured in the original datacube. **Bottom row** in each set: Fluxes measured in the decomposed datacube using CAPIVARA.

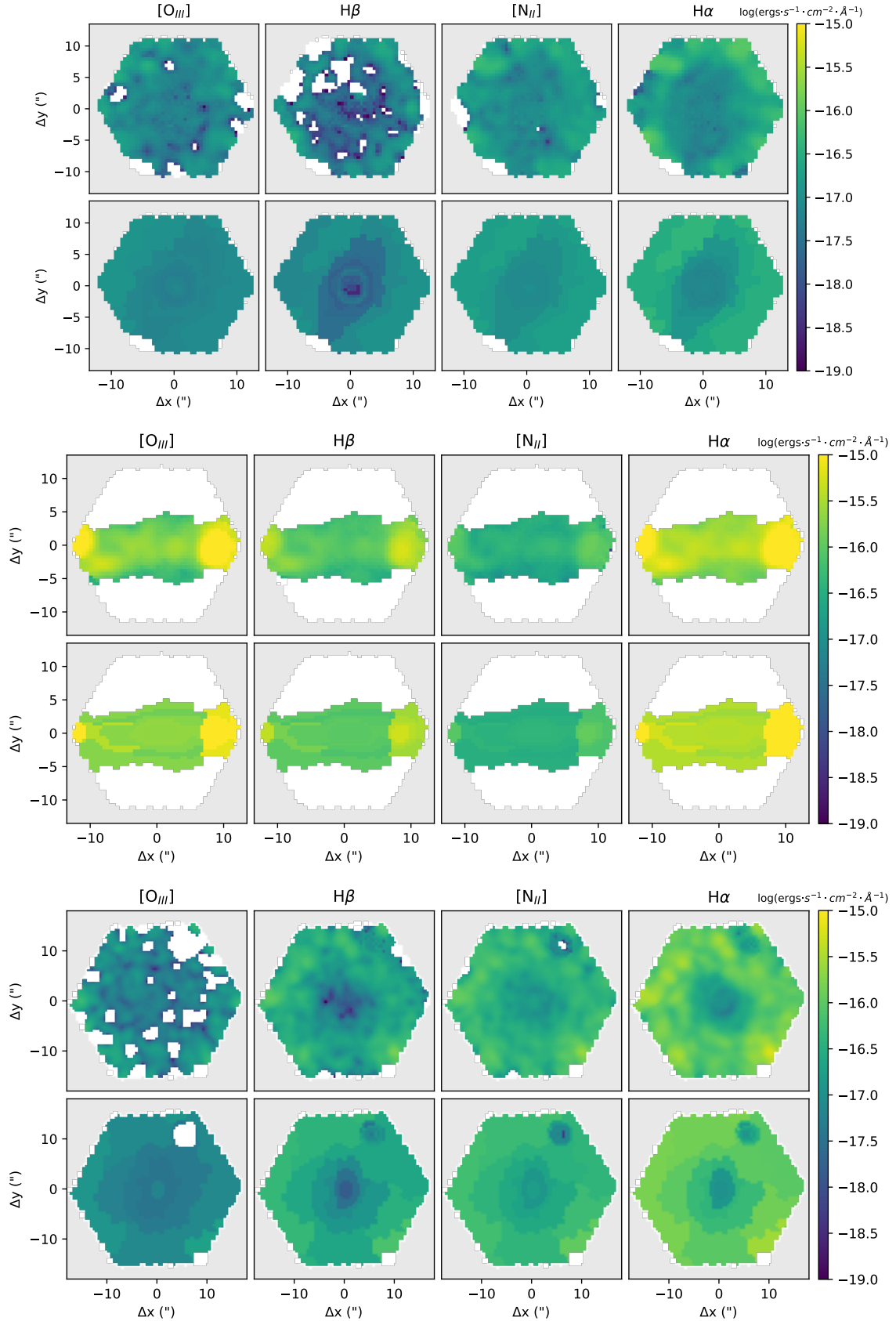


Figure 8. Logarithmic fluxes of the four main emission lines for 8443-6102 (top), 10224-6104 (middle), and 11749-12701 (bottom), in $\text{ergs}\cdot\text{s}^{-1}\cdot\text{cm}^{-2}\cdot\text{\AA}^{-1}$. **Top row** in each set: Fluxes measured in the original datacube. **Bottom row** in each set: Fluxes measured in the decomposed datacube using CAPIVARA.

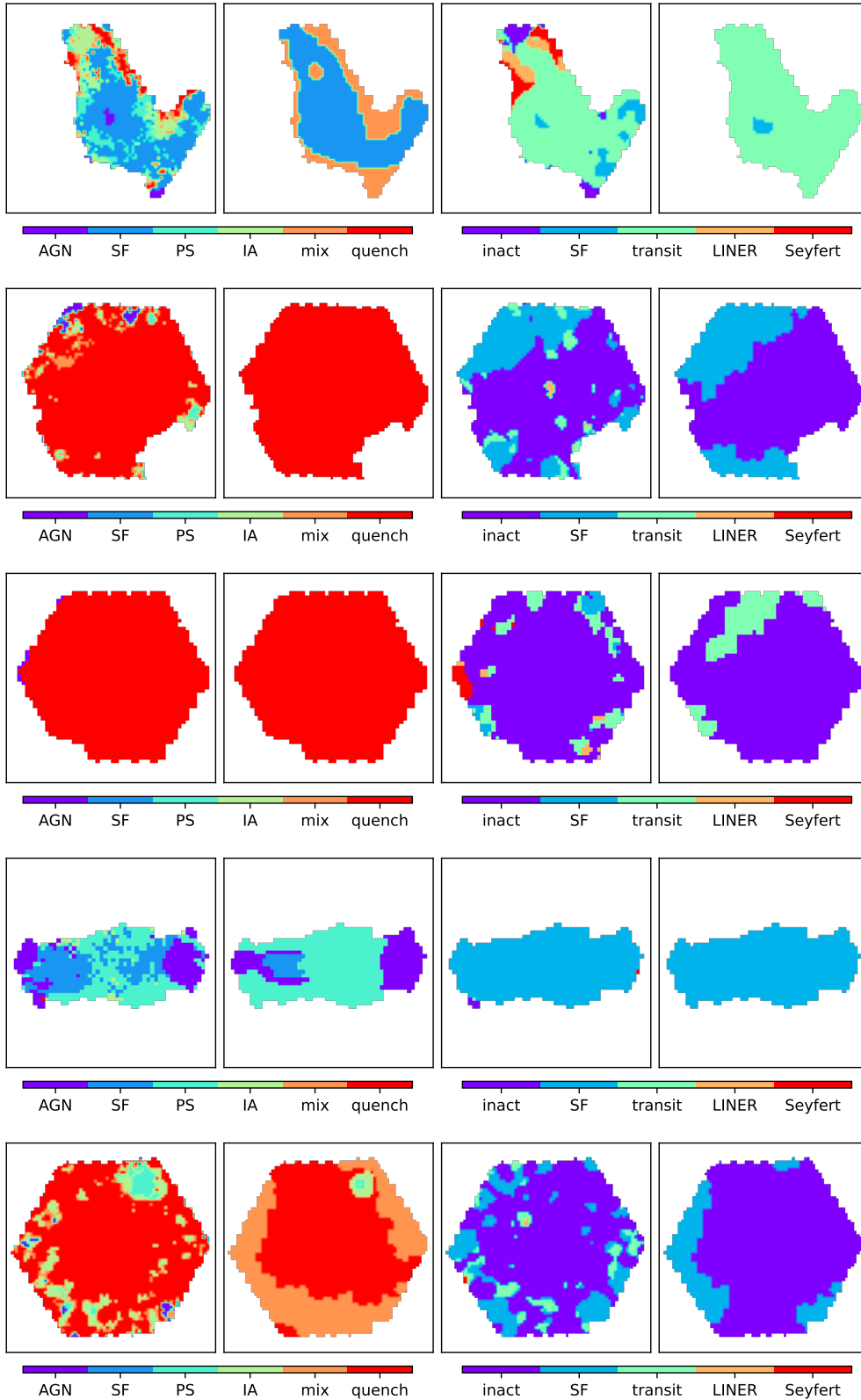


Figure 9. Spectral classification maps for five regions: 7443-12703 (top), 8135-12701 (second from top), 8443-6102 (middle), 10224-6104 (second from bottom), and 11749-12701 (bottom). The first two panels on the left display the maps for the continuum classes, while the two panels on the right present the classification based on emission lines. In each case, the left panels show the analysis on the original datacube, and the right panels show the analysis in the decomposed datacube using *CAPIVARA*.

REFERENCES

- Anders F., et al., 2014, *Astronomy & Astrophysics*, 564, A115
- Ardern-Arentsen A., et al., 2024, *Monthly Notices of the Royal Astronomical Society*, 530, 3391
- Bacon R., et al., 2001, *MNRAS*, 326, 23
- Baker W. M., et al., 2023, arXiv preprint arXiv:2306.02472
- Baldwin J. A., Phillips M. M., Terlevich R., 1981, *PASP*, 93, 5
- Blanton M. R., et al., 2017, *AJ*, 154, 28
- Buitrago F., Trujillo I., Conselice C. J., Bouwens R. J., Dickinson M., Yan H., 2008, *ApJ*, 687, L61
- Bundy K., et al., 2015, *ApJ*, 798, 7
- Cappellari M., Copin Y., 2003, *MNRAS*, 342, 345
- Carnall A. C., et al., 2023, *MNRAS*, 520, 3974
- Carniani S., et al., 2023, arXiv e-prints, p. arXiv:2306.11801
- Casado J., Ascasibar Y., García-Benito R., Guidi G., Choudhury O. S., Bellocchi E., Sánchez S. F., Díaz A. I., 2017, *MNRAS*, 466, 3989
- Chambon H., Fraix-Burnet D., 2024, arXiv e-prints, p. arXiv:2405.16949
- Chiti A., Mardini M. K., Frebel A., Daniel T., 2021, *The Astrophysical Journal Letters*, 911, L23
- Cid Fernandes R., Gu Q., Melnick J., Terlevich E., Terlevich R., Kunth D., Rodrigues Lacerda R., Joguet B., 2004, *MNRAS*, 355, 273
- Cid Fernandes R., Mateus A., Sodré L., Stasińska G., Gomes J. M., 2005, *MNRAS*, 358, 363
- Cimatti A., Fraternali F., Nipoti C., 2019, arXiv e-prints, p. arXiv:1912.06216
- Cocatto L., Fabricius M. H., Saglia R. P., Bender R., Erwin P., Drory N., Morelli L., 2018, *MNRAS*, 477, 1958
- Coelho P., Gadotti D. A., 2011, *ApJ*, 743, L13
- Coelho P., Mendes de Oliveira C., Cid Fernandes R., 2009, *MNRAS*, 396, 624
- Conselice C. J., 2014, *ARA&A*, 52, 291
- Cortese L., Catinella B., Smith R., 2021, *Publications of the Astronomical Society of Australia*, 38, e035
- Di Matteo P., 2016, *Publications of the Astronomical Society of Australia*, 33, e027
- Diehl S., Statler T. S., 2006, *MNRAS*, 368, 497
- Förster Schreiber N. M., et al., 2009, *ApJ*, 706, 1364
- Foster C., et al., 2021, *Publ. Astron. Soc. Australia*, 38, e031
- Häußler B., et al., 2013, *MNRAS*, 430, 330
- Häußler B., et al., 2022, *A&A*, 664, A92
- Hayden M. R., et al., 2015, *The Astrophysical Journal*, 808, 132
- Helmi A., 2020, *Annual Review of Astronomy and Astrophysics*, 58, 205
- Hubble E. P., 1926, *ApJ*, 64, 321
- Imig J., et al., 2023, *ApJ*, 954, 124
- Jegatheesan K., Johnston E. J., Häußler B., Nedkova K. V., 2024, *A&A*, 684, A32
- Johnston E. J., et al., 2017, *MNRAS*, 465, 2317
- Johnston E. J., Häußler B., Jegatheesan K., 2022, *MNRAS*, 514, 6120
- Kauffmann G., et al., 2003, *MNRAS*, 346, 1055
- Kewley L. J., Dopita M. A., Sutherland R. S., Heisler C. A., Trevena J., 2001, *ApJ*, 556, 121
- Kim J.-h., Wise J. H., Alvarez M. A., Abel T., 2011, *The Astrophysical Journal*, 738, 54
- Krajnović D., Cappellari M., de Zeeuw P. T., Copin Y., 2006, *MNRAS*, 366, 787
- Kroupa P., 2001, *MNRAS*, 322, 231
- Krumholz M. R., Burkhardt B., Forbes J. C., Crocker R. M., 2018, *MNRAS*, 477, 2716
- Kullback S., Leibler R. A., 1951, *The Annals of Mathematical Statistics*, 22, 79
- Lah P., Scott N., Barone T. M., Robotham A. S. G., D'Eugenio F., Colless M., Casura S., 2023, *Publ. Astron. Soc. Australia*, 40, e002
- Lani C., et al., 2013, *MNRAS*, 435, 207
- Larson K. L., et al., 2016, *ApJ*, 825, 128
- Law D. R., et al., 2016, *AJ*, 152, 83
- Li W., 1990, *Journal of Statistical Physics*, 60, 823
- Lima-Dias C., et al., 2021, *MNRAS*, 500, 1323
- Lima-Dias C., et al., 2024, *MNRAS*, 527, 5792
- Lin L., et al., 2019, *The Astrophysical Journal*, 872, 50
- López-Corredoira M., Vazdekis A., Gutiérrez C., Castro-Rodríguez N., 2017, *Astronomy & Astrophysics*, 600, A91
- Mallmann N. D., et al., 2018, *MNRAS*, 478, 5491
- Méndez-Abreu J., Sánchez S. F., de Lorenzo-Cáceres A., 2019, *MNRAS*, 484, 4298
- Murtagh F., Legendre P., 2014, *Journal of Classification*, 31, 274
- Nedkova K. V., et al., 2024, arXiv e-prints, p. arXiv:2406.14613
- Ness M., Freeman K., 2016, *Publications of the Astronomical Society of Australia*, 33, e022
- Paszke A., et al., 2019, *Advances in neural information processing systems*, 32
- Peng C. Y., Ho L. C., Impey C. D., Rix H.-W., 2002, *AJ*, 124, 266
- Peng C. Y., Ho L. C., Impey C. D., Rix H.-W., 2010a, *AJ*, 139, 2097
- Peng Y.-j., et al., 2010b, *ApJ*, 721, 193
- Pernet E., Böcker A., Martín-Navarro I., 2024, arXiv e-prints, pp arXiv-2406
- Pietrinferni A., Cassisi S., Salaris M., Castelli F., 2004, *ApJ*, 612, 168
- Pietrinferni A., Cassisi S., Salaris M., Castelli F., 2006, *ApJ*, 642, 797
- Queiroz A. B. A., et al., 2021, *A&A*, 656, A156
- Riffel R., Pastoriza M. G., Rodríguez-Ardila A., Bonatto C., 2009, *MNRAS*, 400, 273
- Rola C. S., Terlevich E., Terlevich R. J., 1997, *MNRAS*, 289, 419
- Rupke D. S. N., Veilleux S., 2013, *ApJ*, 768, 75
- Ruschel-Dutra D., et al., 2021, *MNRAS*, 507, 74
- Samuel J., Wetzel A., Santistevan I., Tollerud E., Moreno J., Boylan-Kolchin M., Bailin J., Pardasani B., 2022, *Monthly Notices of the Royal Astronomical Society*, 514, 5276
- Sánchez S. F., et al., 2004, *ApJ*, 614, 586
- Sánchez S. F., Cardiel N., Verheijen M. A. W., Pedraz S., Covone G., 2007, *MNRAS*, 376, 125
- Sánchez S. F., et al., 2012, *A&A*, 538, A8
- Sánchez S. F., et al., 2016, *Rev. Mex. Astron. Astrofis.*, 52, 21
- Sanders J. S., Fabian A. C., 2001, *MNRAS*, 325, 178
- Sandles L., et al., 2023, arXiv e-prints, p. arXiv:2307.08633
- Schawinski K., et al., 2010, *ApJ*, 711, 284
- Simard L., et al., 2002, *ApJS*, 142, 1
- Stasińska G., 2007, arXiv:0704.0348,
- Storchi-Bergmann T., Raimann D., Bica E. L. D., Fraquelli H. A., 2000, *ApJ*, 544, 747
- Tabor M., Merrifield M., Aragón-Salamanca A., Cappellari M., Bamford S. P., Johnston E., 2017, *MNRAS*, 466, 2024
- Vazdekis A., Koleva M., Ricciardelli E., Röck B., Falcón-Barroso J., 2016, *MNRAS*, 463, 3409
- Veilleux S., Osterbrock D. E., 1987, *ApJS*, 63, 295
- Watkins L., van de Ven G., den Brok M., van den Bosch R. C. E., 2013, *MNRAS*, 436, 2598
- Westfall K. B., et al., 2019, *AJ*, 158, 231
- Whitney A., Ferreira L., Conselice C. J., Duncan K., 2021, *ApJ*, 919, 139
- Wisotzki L., Becker T., Christensen L., Helms A., Jahnke K., Kelz A., Roth M. M., Sanchez S. F., 2003, *A&A*, 408, 455
- Zanatta E., Sánchez-Janssen R., de Souza R. S., Chies-Santos A. L., Blakeslee J. P., 2024, *MNRAS*, 530, 2670
- de Souza R., Thorp S., Galbany L., Ishida E., González-Gaitán S., Schmitz M., Krone-Martins A., Peters C., 2023, *Astronomy and Computing*, 44, 1

This paper has been typeset from a $\text{\TeX}/\text{\LaTeX}$ file prepared by the author.